Mesenchymal stem cell mechanics from the attached to the suspended state: supporting material

Materials and Methods

Cell culture. Primary human mesenchymal stem cells (hMSCs) were obtained from the bone marrow of adult donors (Stem Cell Technologies and ReachBio LLC) and isolated and expanded by density gradient centrifugation and plating on tissue culture polystyrene (TCPS) [1]. PD1 was considered to be the first population doubling after identification of MSC colonies. Cells were cultured at 37°C in a humidified atmosphere at 5% CO_2 in proprietary media (Mesencult complete, basal media #5401 plus supplements #5402, Stem Cell Technologies, supplemented with 2 mM L-glutamine, VWR). Cells were frozen at passages 1 and 2 (P1 and P2) and later thawed, seeded at 2×10^3 cm^{-2}, and expanded to P9 (at which point the typical observed doubling time of two days increased considerably as the cells became senescent). The media was exchanged the day after thawing and every four days thereafter. The cells were passaged (0.05% trypsin / 1 mM EDTA, Gibco) at 80% confluence (approximately every eight days) via a 1:4 split. PDs were determined by counting cell number at seeding with a hemacytometer; each passage corresponded to approximately two PDs. hMSCs from donor 1 were examined by both atomic force microscopy (AFM) and optical stretching (OS). Cells from two additional donors (donors 2 and 3) were examined by OS specifically to investigate possible mechanical changes at PDs ≤ 6. Porcine MSCs (pMSCs) were isolated from porcine bone marrow and cultured in the same way as the hMSCs; these cells were frozen at P2 and later expanded to P8.

These culture conditions are generally believed to avoid widespread differentiation of adult MSCs during long-term expansion subculture [1]. However, we note that some groups report occasional spontaneous osteodifferentiation [2] or increased expression of osteogenetic markers such as osteocalcin in expansion cultures [3], though others see decreased osteocalcin [4] and still others see little change in osteogenic gene expression over multiple passages [5]. Furthermore, we saw no visual or quantitative assay evidence (from inspection of phase contrast images for lipid vacuoles or mineralization, or from standard assays of alkaline phosphastase as an early marker of osteogenesis [1]) that would suggest that a considerable fraction of our MSCs were differentiating toward terminal lineages such as adipocytes or osteoblasts in the absence of deliberate chemical induction.

Atomic force microscopy. AFM images of MSCs, cultured to <80% in 60 mm diameter TCPS dishes, were acquired in contact mode in equal parts HEPES buffer and basal media at 37°C on a commercial scanning probe microscope (3DMFP, Asylum Research, Inc.). Silicon nitride cantilevers (MCLT-AUHW, Veeco) with stiffness $k \approx 10$ pN/nm and probe radius $R = 25$ nm were used and calibrated before each experiment. Cantilever deflection in terms of laser photodiode voltage and cantilever spring constant k were calculated as described by Thompson et al. [6]. Images were acquired at a scanning rate of 200 μm/s, nominal contact force of 0.4–0.8 pN, and resolution ranging from 256×256 to 1024×1024 pixels per image, with up to 150 cells imaged per PD.

We calculated the apparent radius of stress fibers for at least 50 cells per chosen PD. AFM topographic images were analyzed by a script written to calculate the maxima and minima of at least 50 AFM line scans from each cell imaged (Matlab). Indentation force-displacement (F–δ) responses were acquired for at least 50 positions within each cell away from the nucleus, using the same cantilever as for image acquisition, at a rate of 0.5 μm/s. An effective elastic modulus of the indented cell E was estimated by applying the Hertz equation (IgorPro, WaveMetrics) to indentation data collected at locations of similar cell thickness, up to maximum indentation depths of 20 nm. According to the Hertzian-based model for a spherical indenter, the relationship between the applied force F and tip indentation depth δ is given by $F = 4E\delta^{3/2}\sqrt{R}/3(1-\nu^2)$, where E is the elastic modulus and ν is Poisson's ratio (assumed to be 0.5) of the deformed volume (as-

suming the probe material to be comparably rigid). The stiffness E is not intended to be a rigorous measure of the elastic modulus of an entire cell, but provides a quantitative comparison of the effective cytoskeletal stiffness among cells. Local cell height was acquired from the AFM topography images (relative to the TCPS substratum) and was similar for all points used to calculate stiffness.

We acquired multiple AFM indentation measurements to determine a single mean value per passage that could be used to quantify the structural and mechanical changes, if any, observed via AFM profiling, and to compare passages with quantitative mechanical data to enable statistically significant conclusions. A consequence of selecting many random indentation locations of similar cell thickness is the possibility of initiating contact loading that is nearer to or further from stress fibers. We addressed the wide variation in measured stiffnesses across individual cells (where the sample standard deviation is typically comparable to the average value) by using a sufficiently large number of indentation locations (at least 50) and cells (at least 50 per passage).

Microfluidic optical stretching. Cells at approximately 50% confluence in T-25 (25 cm^2) TCPS flasks were treated with 0.05% trypsin / 1 mM EDTA until the cells detached with gentle tapping (approximately 5–10 min). The detachment process was halted by adding complete media, and the suspension was then centrifuged and resuspended in complete media to a cell density of 100–500 K/mL. A syringe containing the cell suspension was attached to a customized syringe rotator that consisted of a 6 rpm DC motor triggered to reverse direction via contact switches. (The effectiveness of syringe rotation at counteracting cell sinking was evaluated separately by counting cell density output from the syringe over 2 h with and without rotation, Fig. S5.) The cells were injected into a hollow square glass capillary (80 μm ID, 160 μm OD) that was positioned between two single-mode optical fibers split from a 1064 nm fiber laser (YLR-3X2-1064, IPG Photonics) [7].

After injection of the cell suspension into the capillary, a microfluidic valve (Upchurch) was used to connect the capillary to adjustable-height reservoirs capable of controlling the flow to bring a single cell to a motionless position between the fibers. Cells were stretched only when the flow was stopped, as any residual flow tends to rotate the cell during stretching. A customized LabView program applied trapping power (0.2 W / 2 s), stretching power (0.9 W / 4 s), and trapping power (0.2 W / 2 s) per fiber to bring the cell to an equilibrium position, deform the cell, and allow recovery, respectively, while simultaneously recording cell images by phase contrast microscopy at 10–15 frames s^{-1}. These laser power values were chosen to ensure measurable cell deformation while minimizing cell heating. (Laser impingement in this configuration results in a temperature increase on the order of 10°C/W [8, 9]; we therefore estimate the 0.9 W stretching power per beam to briefly increase the cell temperature from room temperature to 35–45°C.) The experiment was performed by stretching as many cells as possible in 2 h. Only clumps, severely blebbing cells, and dead cells were not stretched; additionally, in most experiments, every cell (stretched and non-stretched cells) was photographed to provide a visual record consisting of >10,000 images of hMSC morphology in suspension (Fig. S6).

Another customized LabView program was used to detect the edge of the cell by its brightness gradient and then calculate deformation (quantified as the normalized change in diameter) in the direction of the laser beam axis over time [7]. All cells that rotated perceptibly were ruled out, as were cells whose deformation changed by a value of >1% during trapping and cells whose responses suggested rotation (e.g., sudden discontinuities in deformation measurements), as advised by Lincoln [10]. Reported maximum deformation values correspond to the deformation at the end of the 4 s stretching period.

Additional experiments were performed to investigate the influence of different detachment agents on the resulting suspended cell morphology, as smooth surface topography is easier to analyze by machine vision than blebbing topography. These chemical agents included 0.25% trypsin alone, 0.02% EDTA (Versene, Sigma) alone, and the proprietary cell detachment medium Accutase (Sigma), along with the standard treatment, 0.05% trypsin and 1 mM EDTA.

Staining, flow cytometry, and differentiation. The distribution of cytoskeletal F-actin was analyzed via

immunofluorescence staining (FAK100, Chemicon) (Fig. S1). At PD6 at 48 h post-passage, cells were washed three times with phosphate buffered saline (PBS), fixed for 10 min in 4% glutaraldehyde in PBS, permeabilized for 5 min with 0.1% triton-X, and blocked with 1% bovine serum albumin in PBS. Cells were rinsed three times in blocking solution, incubated with 1:2000 TRITC-conjugated phalloidin in permeabilization buffer for 1 h at 25°C, incubated in 1:5000 DAPI in PBS for 5 min, rinsed in PBS, mounted in universal mount (Gibco), and imaged with epifluorescence (Olympus IX81). The morphology of living and fixed hMSCs was also examined by phase contrast microscopy.

Surface markers of hMSCs were investigated by fluorescence activated cell sorting (FACS) of cells tagged with fluorophore-conjugated antibodies. To assess whether the phenotype of the cultured cells changed with increasing passage number, we evaluated the expression of positive hMSC markers SH2 (CD105) and SH4 (CD73) at various PDs. SH2 (#HB-10473) and SH4 (#HB-10745) hybridoma cells lines for antibody production were purchased from ATCC and cultured in Hybricare medium (ATCC) supplemented with 20% fetal bovine serum (Stem Cell Technologies Inc). The cells were maintained at a density of 10^5–10^6 cells per T-25 flask. At sufficient cell numbers, cells were seeded into a spinner flask for approximately 3 weeks. The antibody in the supernatant was purified over a protein G column and dialyzed against PBS. SH2 and SH4 antibodies were labeled with FITC (Sigma F-7250) and separated on a PD-10 sephadex column (Amersham Pharmacia Biotech). For flow cytometric analyses, approximately 10^6 cells were incubated with relevant PE or FITC labeled antibodies at 4°C for 30 min, diluted with PBS, and centrifuged at 600 g. Cells were suspended in approximately 1 mL PBS and standard FACS analysis (Cell Quest software, Becton Dickinson) was conducted.

Differentiation was performed according to protocols described by Mesencult Inc. hMSCs were expanded to PD4 and PD14, then incubated in the presence of either osteoinductive or adipoinductive culture media for two weeks. Differentiation was characterized by alkaline phosphatase activity (an indicator of osteogenesis) and lipid droplet concentration (an indicator of adipogenesis) (Fig. S3).

Data analysis. Differences in stress fiber radius, cytoskeletal stiffness, optical stretching parameters, and marker expression were compared between groups by using Student's t-test, and p-values were calculated by using a null hypothesis of zero difference between data from the the first and last PDs. Comparison of slopes calculated via linear regression (where the p-value were calculated by using a null hypothesis of zero slope) produced the same conclusions. All two-group data were also compared by using Student's t-test. Blebbing cell proportions were compared between populations by using Pearson's chi-square test.

Various phenomenological constitutive equations were considered for the average time-dependent stretching and recovery of cells by OS; candidates included lumped viscoelastic (i.e., spring-dashpot) models along with power law and offset power law models of the form $At^a + B$. Model equations were fit to the data by nonlinear regression (Mathematica) and compared by adjusted r^2 or Akaike Information Criterion (AIC) value [11] to accommodate models with different numbers of fitting variables [12]. As mentioned in the text, the best fit was acquired with an offset power law (Eq. (2)). The fitted stretching and recovery exponents were similar, as discussed in the text; therefore, for several comparisons in this work, the exponent was fitted with the constraint that $a_S = a_R = a$ (i.e., one exponent was fitted to pooled stretching and recovery data).

Because no trend was observed in the overall power-law exponent a or the recovery parameter C with experiment time, as discussed in the text, these parameters are calculated from all experiment times when presented in this work. The comparisons of cell maximum deformation between passages as measured by OS, however, consider only the 581 cells stretched during the second hour of the 2 h experiment, when the cell deformability was insensitive to time.

The standard error of fitted constitutive law parameters was determined by using the bootstrapping technique [13]. Briefly, out of a set of deformation measurements from n different cells, a new set (also of size n) was created by resampling with replacement, and the candidate constitutive equation was fit to the average deformation of this new set. This process (sampling with replacement and fitting) was repeated

1,000×. The standard deviation of the resulting distribution of fitted parameters, multiplied by a factor close to unity ($\sqrt{n/(n-1)}$) is an estimator for the standard error of that same parameter fitted to the original set (Fig. S4) [13].

Cell availability, morphology, and deformation in optical stretching experiments

Optical stretching is a recently developed technique in which single cells are serially advanced through a microfluidic assembly, irradiated to apply a photonic mechanical load, and characterized by quantifying deformation with machine vision. We present here our experiences with cell availability and morphology, as these factors have considerable influence in throughput and image analysis, respectively.

Motorized syringe rotation counteracted cell sinking in the input syringe over time and enabled experiments to proceed for longer times and with an increased number of cells analyzed per experiment (Fig. S5). We typically inject portions of the cell suspension from the syringe multiple times per hour to resupply cells into the capillary. Without syringe rotation, cell sinking (at a terminal speed that we estimate to be 10 μm/s for hMSCs) resulted in few to no cells available after several tens of minutes due to syringe depletion. When using syringe rotation, however, the density of cells available for injection through the capillary to the trap was relatively unaffected over a 2 h experiment.

We observed much variety in the morphology of suspended hMSCs (Fig. S6), which exhibited folds, blebs, and/or filopodia and were sometimes undergoing cytokinesis when detached from TCPS. Dead cells, which were identified by the lack of a white ring shown by phase contrast microscopy of an intact plasma membrane, and clumps of multiple cells were also observed. Single-cell appearance was divided approximately evenly between smooth and folded cells and blebbing cells, with the other morphologies observed only occasionally. Not surprisingly, more clumps of cells were observed when a higher suspension density was used.

Several hundred cells could be accessed in the capillary during a 2 h experiment, which represented approximately 1% of the total number of detached and suspended cells from a T-25 TCPS flask at 50% confluency. Through the process of stretching and analysis, this number was reduced by roughly an order of magnitude by the following constraints: first, clumps and severely blebbing cells were ruled out, and stretching was attempted on single smooth and folded cells only. Second, cells that rotated perceptibly during stretching were also ruled out, as the changing periphery of rotating cell can be mischaracterized as axial elongation during automated image analysis [7]. Third, cells whose periphery could not be accurately fit by edge detection during analysis were ruled out. Approximately 10% of all observed cells satisfied all of these conditions to make up the final data set, which typically contained several tens of cells per flask.

The frequency of cells with visible blebs decreased significantly during the 2 h experiment ($p = 1.3 \times 10^{-5}$): of cells from donor 3 (P1-3), 166/194 cells (i.e., 86% of cells) observed during the first 15 min had visible blebs, compared to 261/474 cells (i.e., 55% of cells) observed during the second hour. Of the cells observed over time without irradiation, blebs did not lead to cell disintegration, which would indicate apoptosis-driven blebbing; instead, blebs dynamically formed and retracted at different membrane locations for many minutes (Video S7). The fraction of blebbing cells was not observably influenced by the chemical detachment mechanism (trypsin, EDTA, Accutase, or trypsin plus EDTA), indicating that blebbing was not caused by a particular chemical agent but was instead a hallmark of recently suspended hMSCs.

The propensity of hMSCs to bleb can hinder certain experiments. For example, we were interested in applying pharmacological cytoskeletal inhibitors to modulate the stiffness of the hMSC actin cortex. However, chemicals such as cytochalasin D, blebbistatin, and ML-7 that inhibit actin (de)polymerization and actomyosin contraction produce suspended hMSCs with detachment-produced blebs that cannot be retracted, as bleb retraction requires actin polymerization followed by actomyosin contraction [14]. The resulting "blebby" surface topography makes image analysis difficult and consequently has prevented efforts to measure suspended hMSC deformability immediately after detachment while chemically modulating

cytoskeletal behavior.

We also briefly discuss the offset constant B found in our stretching power-law fit $\bar{\varepsilon}(t) = At^a + B$. To our knowledge, this constant has not been reported by any groups using contact techniques, but its nonzero value is statistically significant ($B = -1.33 \pm 0.26$) and essentially constant for $t > 0.5$ s (i.e., the offset constant arises and stabilizes during the first 0.5 s of stretching). If the offset is not included in the model, a naive fit of a pure power law ($\bar{\varepsilon}(t) = At^a$) predicts a stretching exponent of $a = 0.37$ from our data, but the actual deformation rate exponent does not match the predicted value of $a - 1$, as it must for a pure power law to apply. It is not clear how this offset arises, or why it would have a negative value that indicates that the deformation is less than would be expected from a pure power law. It is true that deformations at early times in creep experiments (corresponding to high frequencies in oscillation experiments) likely follow a power law with relatively large exponent ~3/4 due to entropic effects becoming dominant [15, 16], and it can be shown that a larger power-law exponent $a' > a$ at earlier times would produce an effective negative offset at later times when fitting $\bar{\varepsilon}(t) = At^a + B$. However, no offset is seen during recovery, not even a smaller value scaled to correspond to the smaller recovery deformation. Other possible effects, such as laser-induced heating, extracellular or intracellular viscosity, or rotation, do not seem to fit the observations of an offset that is negative upon stretching and absent upon recovery. A possible explanation is related to the soft glassy rheology model developed by Sollich and coworkers [17, 18] and suggested by Fabry et al. to apply to cell rheology [19]. In creep compliance experiments, the first measurements obtained from a soft glassy material after a period of inactivity are predicted to correspond to a higher stiffness value (i.e., a lower deformability), as the material's elements have relaxed into relatively deep and stable energy wells from which they are less likely to emerge through deformation [18]. Subsequent measurements during the same creep cycle (and during subsequent creep recovery) are predicted to correspond to lower (and uniform) stiffness values because the material has had no time for similar relaxation. These characteristics match our observations, at least qualitatively. We therefore speculate that the negative offset corresponds to a transient higher effective stiffness (i.e., a lower deformability during $t < 0.5$ s) when the cell is first stretched by a photonic load after time in suspension without physical contact. This explanation is compatible with the lack of offset reported from creep compliance measurements using microplate rheometry [20, 21] and micropipette aspiration [22]; the cells undergo constant physical contact in these techniques and would therefore not undergo the same relaxation process as a freely suspended cell. Pending further investigation of this offset constant, we currently constrain the fitted data to $t > 0.5$ s, as described in Eq. (2).

Optical stretching presents advantages and limitations for characterizing hMSC mechanics

In collecting a large data set describing hMSC deformability, we have recorded numerous observations relevant to the OS technique; in this section we briefly summarize its advantages and disadvantages as identified in this study. There are certainly favorable aspects of investigating MSCs with a tool that accepts these adherent cells in suspension rather than in the attached state. For example, suspended cells can be examined with a higher throughput, made possible by the combination of microfluidic delivery with automated trapping and positioning of cells as they approach the trapping area. (We note that the total quantity of more than 1,200 cells analyzed individually in this work constitutes the largest study of single-cell mechanical response to date.) Mechanics studies by OS could be useful in collecting data to inform the design of other high-throughput cell mechanics testing tools such as microfabricated deformability-based cell sorters [23]. Nevertheless, this technique, at least at the laser power and time scale explored in the current study, does not appear to identify characteristic mechanical markers of hMSCs that are correlated with extended passaging. If no identifiable markers exist in the suspended state, it could be considerably more difficult to separate cells via microfluidic parallel sorting.

OS also desirably allows whole-cell mechanics to be quantified without the complicating effects of physical contact and stress concentrators. Other single-cell rheological techniques such as atomic force mi-

croscopy, bead cytometry, and microplate rheometry all involve cell attachment to a physical surface. This attachment cues cell activity such as focal adhesion and stress fiber formation that may complicate interpretation [24]. Even the use of relatively inert coatings involves cell-substratum contact, albeit minimal. OS, in contrast, is a fully non-contact technique due to its capability of applying a mechanical load photonically. We note, however, that the current analysis approach is sensitive to blebbing cells, whose edges are difficult to detect by machine vision. As discussed earlier, blebs form when the membrane detaches from the cortex; these characteristics have been seen in other cell lines for approximately an hour after the cell is detached from its substratum, but subside as the cell reinforces membrane-cortex links. In the experiments presented in this work, our goal was to stretch the adherent cells as soon as possible after detachment. However, we are currently experimenting with storing the cells in suspension for one hour or more at 37°C and 5% CO_2 before beginning the stretching process in order to avoid stretching during the "blebby" transition period. This revised approach is likely to increase the percentage of analyzable cells.

---

[1] S.P. Bruder, N. Jaiswal, S.E. Haynesworth, et al. Growth kinetics, self-renewal, and the osteogenic potential of purified human mesenchymal stem cells during extensive subcultivation and following cryopreservation. *Journal of Cellular Biochemistry*, 64(2):278–294, 1997.

[2] C.M. DiGirolamo, D. Stokes, D. Colter, D.G. Phinney, R. Class, and D.J. Prockop. Propagation and senescence of human marrow stromal cells in culture: a simple colony-forming assay identifies samples with the greatest potential to propagate and differentiate. *British Journal of Haematology*, 107(2):275–281, 2001.

[3] A. Banfi, A. Muraglia, B. Dozin, M. Mastrogiacomo, R. Cancedda, and R. Quarto. Proliferation kinetics and differentiation potential of ex vivo expanded human bone marrow stromal cells Implications for their use in cell therapy. *Experimental Hematology*, 28(6):707–715, 2000.

[4] M.N. Kozhevnikova, A.S. Mikaelyan, O.V. Payushina, and V.I. Starostin. Comparative characterization of mesenchymal bone marrow stromal cells at early and late stages of culturing. *Biology Bulletin*, 35(2):132–138, 2008.

[5] P.V. Guillot, C. De Bari, F. Dell'Accio, H. Kurata, J. Polak, and N.M. Fisk. Comparative osteogenic transcription profiling of various fetal and adult mesenchymal stem cell sources. *Differentiation*, 76(9):946–957, 2008.

[6] M.T. Thompson, M.C. Berg, I.S. Tobias, M.F. Rubner, and K.J. Van Vliet. Tuning compliance of nanoscale polyelectrolyte multilayers to modulate cell adhesion. *Biomaterials*, 26(34):6836–6845, 2005.

[7] B. Lincoln, S. Schinkinger, K. Travis, F. Wottawah, S. Ebert, F. Sauer, and J. Guck. Reconfigurable microfluidic integration of a dual-beam laser trap with biomedical applications. *Biomedical Microdevices*, 9(5):703–710, 2007.

[8] E.J.G. Peterman, F. Gittes, and C.F. Schmidt. Laser-induced heating in optical traps. *Biophysical journal*, 84 (2):1308–1316, 2003.

[9] S. Ebert, K. Travis, B. Lincoln, and J. Guck. Fluorescence ratio thermometry in a microfluidic dual-beam laser trap. *Imaging*, 78:2272–2278, 2006.

[10] B. Lincoln. *The Microfluidic Optical Stretcher*. PhD thesis, University of Leipzig, 2006.

[11] K.P. Burnham and D.R. Anderson. *Model Selection and Multimodel Inference*. ASA, 2002.

[12] H. Motulsky and A. Christopoulos. *Fitting models to biological data using linear and nonlinear regression: a practical guide to curve fitting*. Oxford University Press, USA, 2004.

[13] M.R. Chernick. *Bootstrap Methods: A Practitioner's Guide*. Wiley New York, 1999.

[14] G.T. Charras, M. Coughlin, T.J. Mitchison, and L. Mahadevan. Life and times of a cellular bleb. *Biophysical Journal*, 94(5):1836–1853, 2008.

[15] L. Deng, X. Trepat, J.P. Butler, E. Millet, K.G. Morgan, D.A. Weitz, and J.J. Fredberg. Fast and slow dynamics of the cytoskeleton. *Nature Materials*, 5(8):636–640, 2006.

[16] D. Stamenović. Two regimes, maybe three? *Nature Materials*, 5:597–8, 2006.

[17] P. Sollich, F. Lequeux, P. Hébraud, and M.E. Cates. Rheology of soft glassy materials. *Physical Review Letters*, 78(10):2020–2023, 1997.

[18] S.M. Fielding, P. Sollich, and M.E. Cates. Aging and rheology in soft materials. *Journal of Rheology*, 44:323, 2000.

[19] B. Fabry, G.N. Maksym, J.P. Butler, M. Glogauer, D. Navajas, and J.J. Fredberg. Scaling the microrheology of

living cells. *Physical Review Letters*, 87(14):148102, 2001.

[20] N. Desprat, A. Richert, J. Simeon, and A. Asnacios. Creep function of a single living cell. *Biophysical Journal*, 88(3):2224–2233, 2005.

[21] M. Balland, N. Desprat, D. Icard, S. Féréol, A. Asnacios, J. Browaeys, S. Hénon, and F. Gallet. Power laws in microrheology experiments on living cells: Comparative analysis and modeling. *Physical Review E*, 74(2): 21911, 2006.

[22] E.H. Zhou, S.T. Quek, and C.T. Lim. Power-law rheology analysis of cells undergoing micropipette aspiration. *Biomechanics and Modeling in Mechanobiology*, pages 1–10, 2010.

[23] H. Bow, H.W. Hou, S. Goldfless, P. Abgrall, K. Tan, J. Niles, C.T. Lim, and J. Han. Continuous-flow deformability-based sorting of malaria-infected red blood cells. In *MicroTAS*, pages 1219–1221, 2009.

[24] B. Fabry, G.N. Maksym, J.P. Butler, M. Glogauer, D. Navajas, N.A. Taback, E.J. Millet, and J.J. Fredberg. Time scale and other invariants of integrative mechanical behavior in living cells. *Physical Review E*, 68(4):41914, 2003.

Supplemental Figures

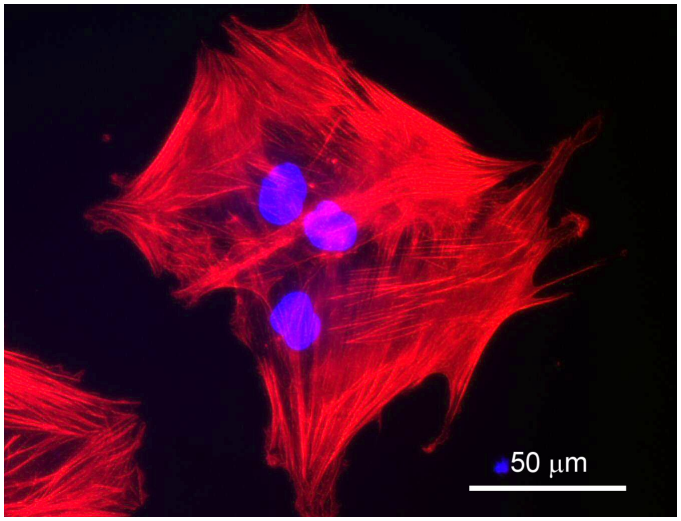

FIG. 1: (Supplemental) Staining of chemically fixed hMSCs confirms that the cytoskeletal networks detected by AFM consisted of F-actin in the form of stress fibers (red = rhodamine phalloidin stain for actin; blue = DAPI stain for DNA).

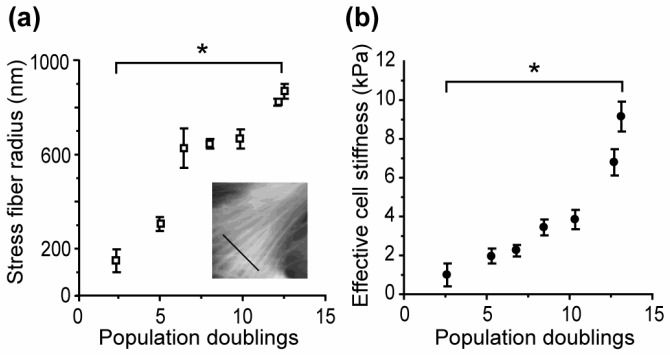

FIG. 2: (Supplemental) Trends of (a) cytoskeletal coarsening and (b) stiffening were also observed in porcine MSCs expanded for 13 PDs on TCPS ($p < 10^{-4}$, n = 43–66 cells per PD). (Data shown as mean ± standard deviation.)

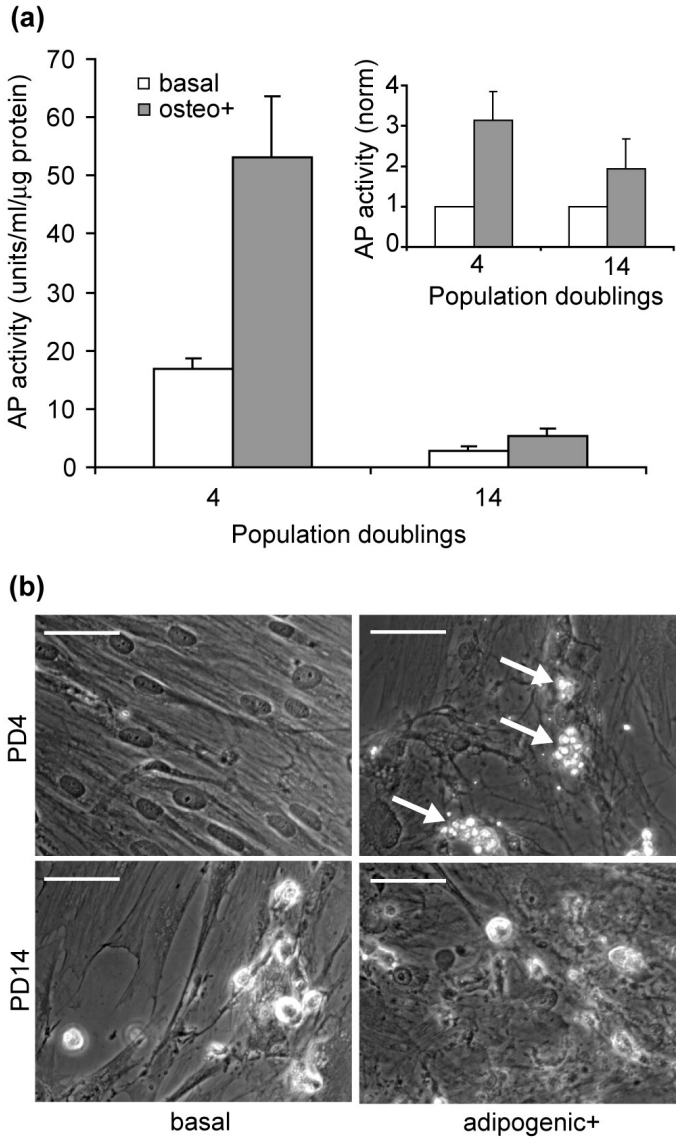

FIG. 3: (Supplemental) (a) Decreased alkaline phosphatase activity (an indicator of osteogenic differentiation) and (b) lipid vacuole formation (an indicator of adipogenic differentiation) after exposure to inductive media were observed with extended passaging (scale bar = 50 μm, data shown as mean ± standard deviation). Inset in (a), alkaline phosphatase activity of osteo-induced cultures relative to basal cultures.

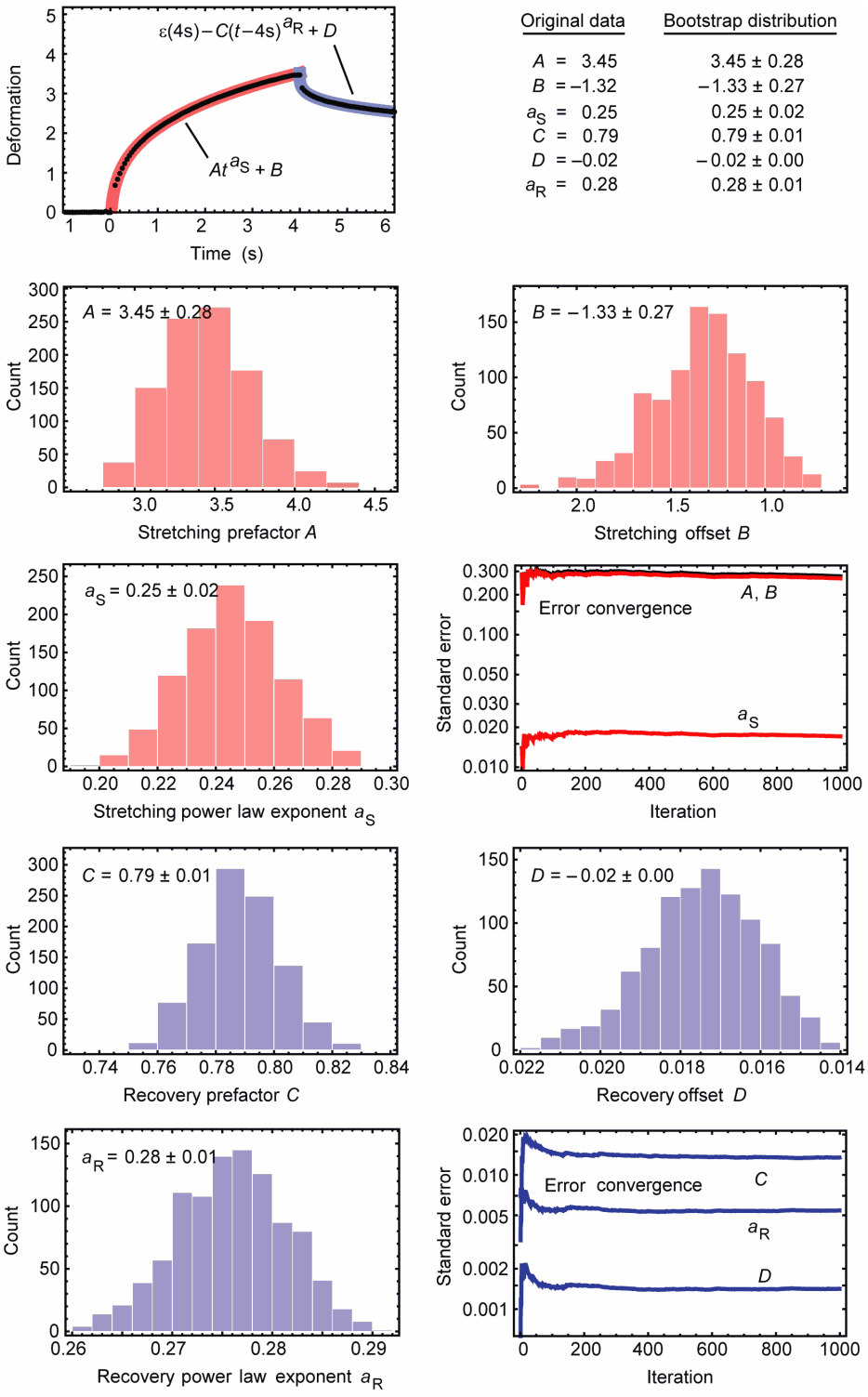

FIG. 4: (Supplemental) The standard error of fitted parameters was determined by using the bootstrapping technique, which resamples the n existing data points (here, individual cells) with replacement and recalculates parameters of interest over multiple iterations. The standard deviation of each parameter's bootstrapped distribution, multiplied by a factor close to unity ($\sqrt{n/(n-1)}$), is an estimator for the standard error of the original parameter. All values converged suitably within 1,000 iterations. Additionally, the means of the bootstrapped distributions matched the original parameters, indicating negligible estimator bias. The parameter D represents the recovery offset considered to be negligible, as discussed in the text.

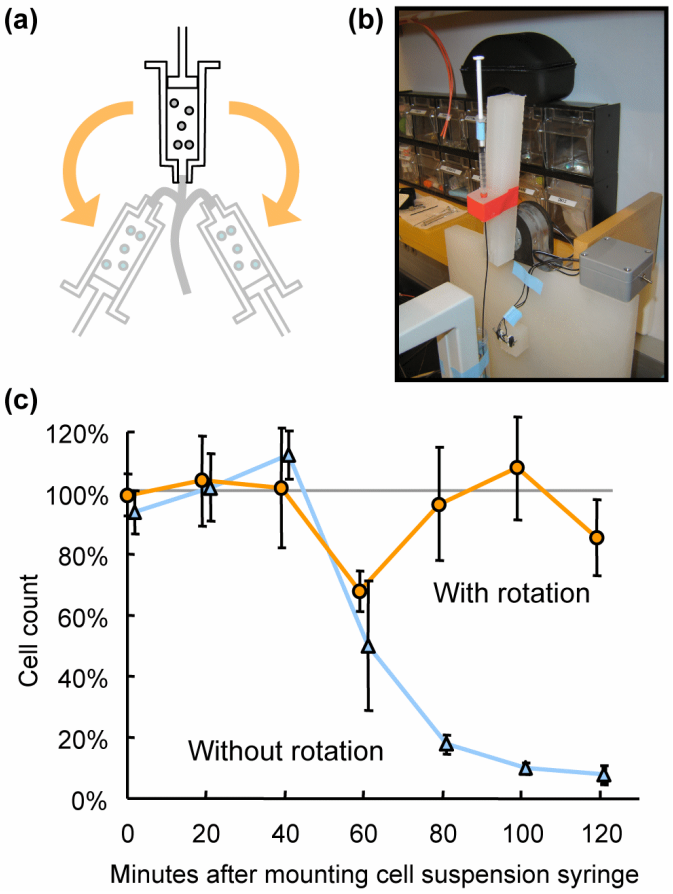

FIG. 5: (Supplemental) A syringe containing the cell suspension was attached to a customized 6 rpm syringe rotator ((a) schematic and (b) photograph) to prevent cell settling. (c) Syringe rotation ensured cell availability during the 2 h stretching experiments; without rotation, the syringe became depleted of suspended cells within approximately 1 h.

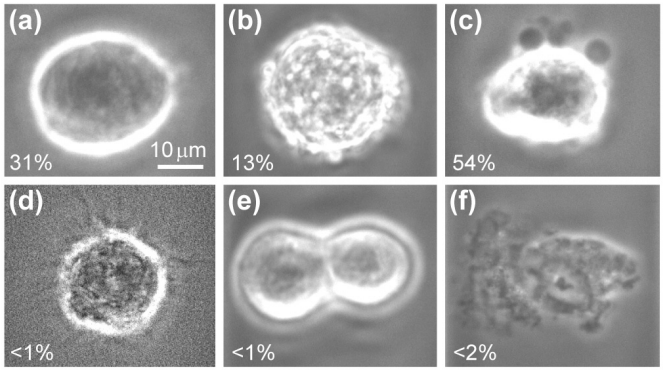

FIG. 6: (Supplemental) Suspended hMSCs exhibit surface morphology variety including (a) smooth cells and cells with (b) folds/ruffles, (c) blebs, and (d) filopodia (image sharpness enhanced to show features more clearly); also occasionally observed are (e) cells undergoing cytokinesis and (f) dead cells, along with clumps of cells. Smooth, ruffled, and blebbing cells are most frequently observed (frequencies shown), and smooth and ruffled cells and cells with filopodia are most amenable to automated edge detection during analysis.

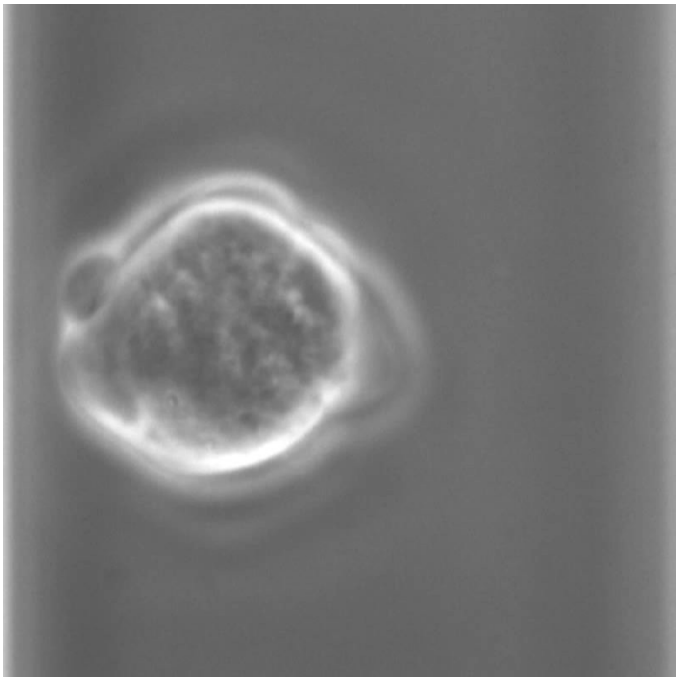

FIG. 7: (Supplemental video) OS at a relatively low (trapping) laser power enables observation of dynamic blebbing in a suspended adherent cell. Repeatedly and at different locations on the cell surface, membrane detachment from the cortex is followed by cytosol streaming into the newly formed bleb, followed by actin polymerization and new cortex formation inside the membrane and bleb retraction driven by actomyosin contraction. (Video sped up 30×.)